Morphology of nanoporous glass: Stochastic 3D modeling, stereology and the influence of pore width

Matthias Neumann [1,*,†] Phillip Gräfensteiner [1,*] Cristine Santos de Oliveira,[2] Juliana Martins de Souza e Silva,[2,3]
Sharon Koppka [4] Dirk Enke,[4] Patrick Huber [5,6,7] and Volker Schmidt [1]

[1]*Institute of Stochastics, Ulm University, Helmholtzstrasse 18, 89069 Ulm, Germany*
[2]*Institute of Physics, Martin-Luther-University Halle-Wittenberg, Von-Danckelmann-Platz 3, 06120 Halle (Saale), Germany*
[3]*Fraunhofer Institute for Microstructure of Materials and Systems IMWS, Walter-Hülse-Strasse 1, 06120 Halle (Saale), Germany*
[4]*Institute of Chemical Technology, Leipzig University, Linnéstrasse 3, 04103 Leipzig, Germany*
[5]*Institute for Materials and X-Ray Physics, Hamburg University of Technology, Denickestrasse 15, 21073 Hamburg, Germany*
[6]*Centre for X-ray and Nano Science CXNS, Deutsches Elektronen-Synchrotron DESY, 22603 Hamburg, Germany*
[7]*Center for Hybrid Nanostructures CHyN, University of Hamburg, Luruper Chaussee 149, 22671 Hamburg, Germany*

Excursion sets of Gaussian random fields are used to model the three-dimensional (3D) morphology of differently manufactured porous glasses (PGs), which vary with respect to their mean pore widths measured by mercury intrusion porosimetry. The stochastic 3D model is calibrated by means of volume fractions and two-point coverage probability functions estimated from tomographic image data. Model validation is performed by comparing model realizations and image data in terms of morphological descriptors which are not used for model fitting. For this purpose, we consider mean geodesic tortuosity and constrictivity of the pore space, quantifying the length of the shortest transportation paths and the strength of bottleneck effects, respectively. Additionally, a stereological approach for parameter estimation is presented, i.e., the 3D model is calibrated using merely two-dimensional (2D) cross-sections of the 3D image data. Doing so, on average, a comparable goodness of fit is achieved as well. The variance of the calibrated model parameters is discussed, which is estimated on the basis of randomly chosen, individual 2D cross-sections. Moreover, interpolating between the model parameters calibrated to differently manufactured glasses enables the predictive simulation of virtual but realistic PGs with mean pore widths that have not yet been manufactured. The predictive power is demonstrated by means of cross-validation. Using the presented approach, relationships between parameters of the manufacturing process and descriptors of the resulting morphology of PGs are quantified, which opens possibilities for an efficient optimization of the underlying manufacturing process.

I. INTRODUCTION

Porous glass (PG) is characterized by a precisely controllable mean pore width, a narrow distribution of pore widths as well as a regular interconnected pore structure [1]. By manufacturing nano-PGs, three-dimensional (3D) reaction spaces with mean pore widths ranging from a few (∼2 nm) to several thousand nanometers can be designed [2]. In the pore system, interactions between different substances as well as interactions of substances with the pore wall can be investigated. This is of particular interest for mechanistic studies on the interaction, flow, and diffusion of liquids as a function of their complexity [3–5] as well as biologically active substances, e.g., for enzymes, viruses, bacteria, catalytic reactions, and protein dynamics [6–8]. Moreover, PG can be used as a reservoir, e.g., for storage and sustained release of drugs [9].

PGs are produced in two ways: by the sol-gel [10] and the controlled PG (CPG) process, also known as the Vycor process [11]. In both cases, phase separation is induced in a homogeneous mixture. The separation can be chemically initiated in the case of sol-gel materials or thermally initiated in CPG. The resulting porosity and pore width are mainly controlled by three factors, namely, the composition of the homogeneous mixture as well as time and temperature of phase separation. In the case of CPG, the aim of phase separation is to create two chemically different phases with an interconnected structure, where one of the phases has a composition of >96 mol. % SiO_2. Due to different solubility, the nonsilicate-rich phase can be dissolved, resulting in an open porous 3D SiO_2 component after a cleaning and drying step [12,13]. Since these pore structures can be reproducibly manufactured with high accuracy regarding the pore width, PGs are used as calibration materials for standard pore structure analytics such as nitrogen adsorption and mercury intrusion. Furthermore, they are suitable as a model system to investigate volume and surface effects on crystallisation and diffusion processes [14–18].

In addition to porosity and mean pore width, further morphological descriptors of the transport phase, i.e., the pore space in our case, have a strong influence on physical prop-

---

*These authors contributed equally to this work.
†matthias.neumann@uni-ulm.de

erties such as, e.g., effective diffusivity. Thus, a quantitative understanding of relationships between parameters of the manufacturing process, morphological descriptors of the 3D nanostructure, and physical materials properties is required to generate nano-PGs with predefined morphological and physical properties. Note that this kind of morphological influence has been quantified for porous silica manufactured by sol-gel processes in Ref. [19] as well as for larger classes of porous or composite materials in Refs. [20–24].

In this paper, we use stochastic 3D modeling to generate digital twins of 3D image data representing the morphology of nano-PG. In this way, we can quantify the influence of mean pore width, measured by mercury intrusion porosimetry and adjustable during the manufacturing process, on further morphological descriptors that are experimentally not accessible. For the latter, we consider descriptors for the length of transportation paths and the strength of bottleneck effects, which in turn have a strong influence on physical transport properties, like effective diffusivity [22] and liquid imbibition [25,26], where we consider three CPGs with different mean pore widths and one silica monolith manufactured as described in Refs. [27,28], respectively.

Our modeling approach is based on excursion sets of Gaussian random fields, see chap. 16 in Ref. [29]. This means that the model can be directly calibrated to the materials morphology observed in 3D image data instead of modeling the movement of atoms and molecules during the manufacturing process. Thus, the presented approach conceptually differs from previous models for CPGs, which use molecular dynamics simulations [30,31]. Note that excursion sets of Gaussian random fields have been exploited to model the morphology of various functional materials, such as electrodes in solid oxide fuel cells [32–35], electrodes in gas-diffusion electrodes [36], aerogels [37], concrete [38], nanoporous gold [39], and Vycor glass [40]. The excursion set model used in this paper allows for statistically mimicking the 3D nanostructure of the considered glasses with only three model parameters. Model validation is performed by comparing morphological descriptors of simulated and measured image data, which have not been used for model fitting. Since our model calibration is based on 3D image data, the acquisition of which is costly and time consuming, we also show how to use two-dimensional (2D) cross-sections to stereologically estimate the model parameters. Moreover, we discuss the quality of these estimates in detail. In this paper, we use excursion sets of Gaussian random fields, as the microstructures represented in image data look rather similar to realizations of such excursion set models. This visual impression is formally justified by the model validation, where good accordance between model realizations and data is observed. However, note that, for morphologically different microstructures or nanostructures, there are further 3D models available in the literature allowing for an efficient model fitting based on 2D data. In addition to models from stochastic geometry and mathematical morphology [29,41,42], this includes, e.g., machine-learning approaches [43], simulated and hierarchical annealing [44,45] as well as approaches based on phase retrieval [46].

Furthermore, we use the model to quantify relationships between mean pore width of the glasses and their morphology. For this purpose, we perform interpolations in the parameter space; we can predict the morphology of CPGs with mean pore widths that have not been investigated by 3D imaging or that have not even been manufactured so far. Thus, the presented data-driven modeling approach provides a framework to generate a comprehensive database of virtual (but nevertheless realistic) nano-PGs, which in future work can be used as an input for numerical simulations of effective physical properties, such as considered, e.g., in Refs. [25,47]. This allows us, in addition to investigating relationships between parameters of the manufacturing process and descriptors of the resulting morphology, to quantitatively study relationships between morphology and physical materials properties with a reduced experimental effort.

In other words, in this paper, we present the following four main topics: (i) Model validation is performed with respect to transport-relevant microstructure descriptors such as constrictivity and geodetic tortuosity, which is not standard in the literature and provides additional insight into the goodness of model fit, particularly with respect to its applicability for investigating relationships between morphology and transport. (ii) A detailed analysis is performed of how the variance of the estimated model parameters behaves in the case of estimation from single 2D image cross-sections and particularly how this affects tortuosity and constrictivity. (iii) Furthermore, the discussion provided regarding the choice of covariance functions of the underlying Gaussian random fields is also an important contribution to the state of the art. In the literature (see for example, Ref. [39]), it is assumed that spinodally decomposed materials can be modeled by covariance functions of the form $\rho(h) = \sin(ah)/ah$, for some parameter $a > 0$. However, our data-driven approach shows that the microstructures considered in this paper cannot be modeled sufficiently well with these kinds of covariance functions. (iv) Last but not least, using interpolation in the space of model parameters, we can predict the overall morphology of nano-PGs with different pore sizes. Cross-validation shows that our approach works well.

The rest of this paper is organized as follows. Descriptions of materials and 3D imaging are provided in Sec. II. Then in Sec. III, the stochastic 3D model for the generation of digital twins of nano-PGs as well as its calibration to 3D image data is explained. The estimation of model parameters based on 2D cross-sections is discussed in Sec. IV. In Sec. V, relationships between parameters of the manufacturing process and descriptors of the 3D morphology are investigated, which is the basis for the predictive simulation of nano-PGs not yet observed by 3D imaging. Finally, Sec. VI concludes.

II. MATERIALS AND 3D IMAGING

A. Description of materials

CPGs in the shape of thin plates with mean pore widths of 100, 150, and 200 nm were prepared as follows. Glass blocks with compositions in the Vycor range ($7Na_2O$–$23B_2O_3$–$70SiO_2$ in wt. %) are heated at $570\,°C < T < 700\,°C$ for 8 h to induce phase separation, which determines the morphology of the pore system. These blocks are then cut into rectangular cuboids with a size of $25 \times 25 \times 0.1$ mm using a diamond saw. Ultra-thin plates are extracted in 1 N HCl at $90\,°C$ for 1 h to
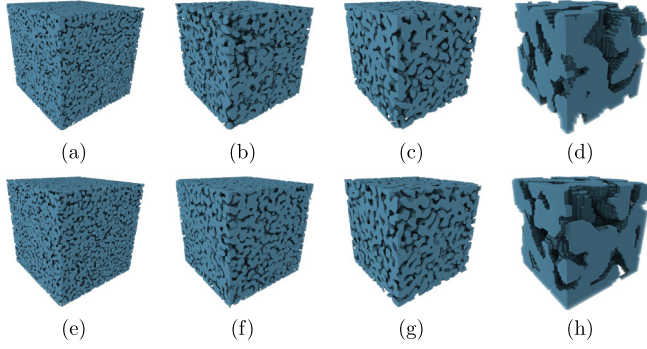
FIG. 1. Top row: Three-dimensional (3D) renderings of tomographic image data representing cubic cutouts (with a side length of 4.8 μm) of the samples (a) CPG100, (b) CPG150, (c) CPG200, and (d) CPG1000. Bottom row: Digital twins drawn from the models fitted to (e) CPG100, (f) CPG150, (g) CPG200, and (h) CPG1000. This visualization shows cutouts of equal physical size and does not cover all available image data, cf. Table I.

TABLE I. Summary of conditions (exposure time t_{exp}, voxel size ϑ, size of the sampling window W in voxel) under which 3D imaging was performed.

Sample	t_{exp}	ϑ	Size of W (voxel)
CPG100	100	16 nm	643×595×529
CPG150	80	32 nm	350×316×504
CPG200	70	32 nm	362×317×420
CPG1000	75	128 nm	358×314×310

plate. In the imaging experiments, a total of 901 projections was obtained over 180° with exposure time t_{exp} and detector binning depending on the given sample, see Table I. Image reconstruction was performed by the filtered backprojection algorithm [48] implemented in the software XMReconstructor, which is part of the Xradia 810 Ultra.

The commercial software Thermo Scientific Avizo (version 9.4.0) was used for image preprocessing. First, a nonlocal means filter as described in Ref. [49] is applied in 3D with a fixed search window of 21×21×21 and a cubic similarity neighborhood of 5×5×5 voxel, where the similarity factor is chosen to be 1. The segmentation of image data, i.e., the classification of each voxel as either pore or solid, was performed using the auto threshold module in Avizo with the IsoData criterion. Note that this Avizo module was also used in Ref. [50] for the segmentation of image data representing glass foams. For CPG200 as an example, a comparison between the grayscale image after noise reduction by filtering and the segmented image is shown in Fig. 2.

III. STOCHASTIC 3D MODELING

We now present a stochastic model for mimicking the 3D morphology of the nano-PGs described in Sec. II A. The modeling idea, together with some fundamental formulas, is stated in Sec. III A. These formulas are then used in Sec. III B for the calibration of model parameters. In Sec. III C, a physicochemical interpretation is given for the parametric covariance model considered in Sec. III B. Furthermore, model validation is explained in Sec. III D, where morphological descriptors

dissolve the borate-rich phase, followed by a 1 h treatment with 0.5 N NaOH at room temperature to remove dispersed silicates. The resulting CPG plates are neutral washed and air-dried overnight between each leaching step. For more information, see Ref. [27]. Additionally, a silica monolith with a mean pore width of 1000 nm was prepared via a sol-gel process using the procedure reported in Ref. [28]. The mean pore widths have been determined by means of mercury intrusion porosimetry. For the 1000 nm sample, a solution of urea and polyethylene oxide (PEO) was prepared in distilled water under vigorous stirring for 30 min at room temperature. Afterwards, sulfuric acid and tetraethoxysilane (TEOS) were added. Then after an additional 30 min of vigorous stirring, the mixture was poured into a polytetrafluoroethylene (PTFE)-lined stainless steel autoclave. The reaction mixture, consisting of 17 g of H_2O, 4.21 g of urea, 2.20 g of PEO, 2.52 g of H_2SO_4, and 15.51 g of TEOS, was submitted to thermal treatment. In a first step, gelation was performed at 40–50 °C for 24 h. In a second step, hydrothermal treatment was performed at 120 °C for 20 h. After cooling, the wet gel obtained was removed from the autoclave and washed with water until the pH was neutral. The wet gel was then submerged in water inside a plastic tube and dried at 120 °C for 24 h. Thereafter, the xerogel obtained was calcined at 600 °C for 8 h, using a heating rate of 3 °Cmin^{-1} starting from room temperature. In the following, we denote the samples described above by CPG100, CPG150, CPG200, and CPG1000, respectively, depending on the corresponding mean pore width, see Fig. 1 for visualizations of tomographic image data and corresponding model realizations.

B. 3D imaging and image preprocessing

Imaging experiments were performed with an x-ray microscope Zeiss Xradia 810 Ultra that operates with a chromium x-ray source (5.4 keV) using phase-contrast imaging mode. For this purpose, a gold phase ring, with a thickness designed to produce a phase shift of $3\pi/2$ of the nondiffracted x-ray beam, was positioned near the back focal plane of the zone
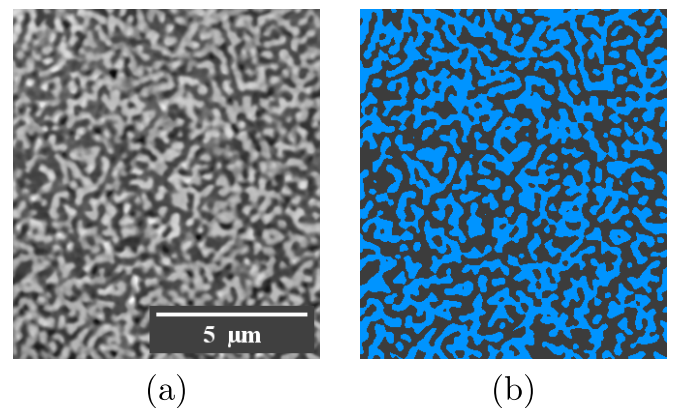

FIG. 2. (a) Two-dimensional (2D) cross-section of the grayscale image of sample CPG 200 after noise reduction by filtering and (b) the corresponding segmented cross-section, where the solid phase is represented in blue and the pore space in dark gray.

not used for model calibration are compared with each other for image data of real and simulated nano-PGs.

A. Model description and some fundamental formulas

The solid phase of the nano-PGs is modeled by motion-invariant (i.e., stationary and isotropic) excursion sets of Gaussian random fields, see also Refs. [29,41,42]. For an introduction to Gaussian random fields and their geometric properties, we refer to Refs. [41,51]. The assumption of motion invariance is justified, as there is no preferred direction in the manufacturing process. Moreover, this assumption is confirmed on image data by use of the chord-length distributions [see sec. 6.3.4 in Ref. [41]], provided in the Appendix. Consider a motion-invariant Gaussian random field $X = \{X(u) : u \in \mathbb{R}^3\}$ such that $\mathbb{E}X(u) = 0$ and $\mathsf{Var}X(u) = 1$ for each $u \in \mathbb{R}^3$. Let $\rho : \mathbb{R}^3 \times \mathbb{R}^3 \to \mathbb{R}$ denote the covariance function of X, i.e., $\rho(u, v) = \mathsf{Cov}(X(u), X(v))$ for all $u, v \in \mathbb{R}^3$. Note that, by the motion invariance of X, the value $\rho(u, v)$ does only depend on the distance $|u - v|$ between $u, v \in \mathbb{R}^3$. Hence, with some abuse of notation, we write $\rho(h) = \rho(u, v)$ for any $h \in [0, \infty)$, where $u, v \in \mathbb{R}^3$ are arbitrary points in the 3D Euclidean space $\mathbb{R}^3$, with $h = |u - v|$.

By considering the (random) subset of $\mathbb{R}^3$, where the random field X exceeds a predefined value $\lambda \in \mathbb{R}$, we obtain a so-called excursion set $\Xi = \{u \in \mathbb{R}^3 : X(u) > \lambda\}$, which is then used to model the solid phase of the CPGs. Note that, under the conditions mentioned above, the distribution of X depends only on the covariance function $\rho : \mathbb{R}^3 \times \mathbb{R}^3 \to \mathbb{R}$. Thus, the distribution of the random set Ξ is uniquely defined by ρ and the threshold $\lambda \in \mathbb{R}$. This means that to properly calibrate the model, ρ and λ must be estimated based on information from the 3D image data described in Sec. II B.

For this purpose, we make use of some fundamental formulas, which are true for volume fractions and two-point coverage probability functions of excursion sets of motion-invariant Gaussian random fields. First, we consider the volume fraction $\varepsilon = \mathbb{E}(\nu_3(\Xi \cap [0, 1]^3))$ of the stationary random set Ξ, where ν_3 denotes the 3D Lebesgue measure. It can be easily shown that $\varepsilon = \mathbb{P}(X(o) > \lambda)$, where $o \in \mathbb{R}^3$ denotes the origin. Thus, we get that

$$\varepsilon = 1 - \Phi(\lambda), \tag{1}$$

where $\Phi : \mathbb{R} \to [0, 1]$ denotes the distribution function of the standard normal distribution. We can therefore estimate the threshold λ through Eq. (1) by estimating the volume fraction ε from 3D image data, see Sec. III B below.

Moreover, we consider the two-point coverage probability function $C : [0, \infty) \to [0, 1]$ of Ξ, which is defined by $C(h) = \mathbb{P}(o \in \Xi, u \in \Xi)$ for each $h \geqslant 0$, where $u \in \mathbb{R}^3$ is an arbitrary point, with $|u| = h$. Note that the random excursion set Ξ inherits its motion invariance from the corresponding property of the underlying random field X. Furthermore, the two-point coverage probability function C of Ξ can be expressed via an analytical formula by the covariance function ρ of X, where

$$C(h) = \varepsilon^2 + \frac{1}{2\pi} \int_0^{\rho(h)} \frac{\exp\left(-\frac{\lambda^2}{1+z}\right)}{\sqrt{1 - z^2}} \, dz, \tag{2}$$

for each $h \in [0, \infty)$, see proposition 16.1.1 of Ref. [29].

TABLE II. Estimates for volume fraction and model parameters.

Sample	$\widehat{\varepsilon}$	$\widehat{\lambda}$	$\widehat{a}$ [1/μm]	$\widehat{b}$ [1/μm²]
CPG100	0.503	−0.007520	26.88	38.20
CPG150	0.503	−0.007520	19.28	14.87
CPG200	0.487	0.03259	15.32	5.813
CPG1000	0.460	0.1004	3.900	1.270

B. Model calibration by 3D image data

The procedure for calibrating the level-set model Ξ described in Sec. III A is as follows. We first compute an estimator $\widehat{\varepsilon}$ for the volume fraction ε of Ξ from image data, as described in Sec. 6.4.2 of Ref. [41]. Then in view of Eq. (1), an estimator for λ is given by

$$\widehat{\lambda} = \Phi^{-1}(1 - \widehat{\varepsilon}). \tag{3}$$

Numerical results for $\widehat{\varepsilon}$ and $\widehat{\lambda}$, which have been obtained for the four samples CPG100, CPG150, CPG200, and CPG1000, are shown in Table II.

To obtain an estimator $\widehat{C}$ for C, we use an algorithm based on the fast Fourier transform, as described in sec. 6.2.3 of Ref. [52]. This algorithm makes use of the assumption of isotropy by averaging over differently oriented vectors of length h when estimating $C(h)$ for arbitrary $h \in [0, \infty)$. Since the Fourier transform assumes that the underlying image data is periodic, there are often undesirable boundary effects. To avoid this, we first mirror the segmented image data along the facets of the cubic sampling window W in the three axis directions of $\mathbb{R}^3$ before estimating C. This increases the volume of the sampling window by a factor of 8 but removes artifacts of the boundary in the Fourier domain. Note that, for any $h \in [0, \infty)$, the right-hand side of Eq. (2) is strictly increasing in $\rho(h)$. Thus, after replacing $C(h)$, ε, and λ with their respective estimators, we can solve Eq. (2) for $\rho(h)$ numerically using the method of bisection for every $h \in [0, \infty)$. This gives us a nonparametric estimator $\widehat{\rho}$ for ρ. The estimator $\widehat{\rho}$ is then used as a basis for a parametric covariance model. It turns out that a good fit can be achieved by assuming that ρ is of the form:

$$\rho(h) = \frac{\sin(ah)}{ah} \exp(-bh^2), \tag{4}$$

for each $h \in (0, \infty)$ and some parameters $a, b > 0$, see Fig. 3.

Here, one can observe that the location of the minimum of $\widehat{\rho}$ is closely related with the mean pore width of the respective sample. The estimators $\widehat{a}$ and $\widehat{b}$ for the parameters a and b are obtained by using a least-squares approach to fit a function $\widehat{\rho}_{\widehat{a},\widehat{b}}$ of the form given in Eq. (4) to the (nonparametrically) estimated covariance function $\widehat{\rho}$, see Table II. Recall that the latter one is numerically computed by means of Eq. (2), using the two-point coverage probabilities $\widehat{C}(h)$ directly estimated from image data. Virtual glass morphologies generated by the calibrated stochastic 3D model and cutouts of the corresponding tomographic image data are visualized in Fig. 1. For simulating Gaussian random fields, we use the Fourier approach described in Sec. 7 of Ref. [32].
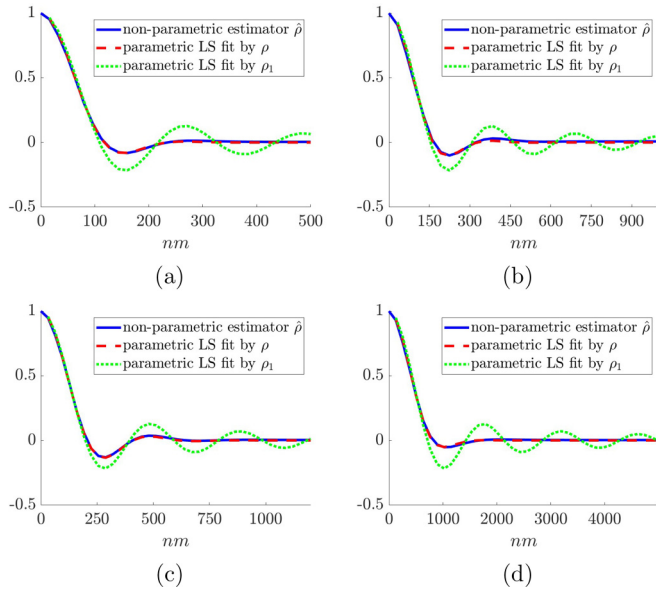
FIG. 3. Nonparametric estimator $\widehat{\rho}$ (blue) for the covariance function ρ, computed for (a) CPG100), (b) CPG150, (c) CPG200, and (d) CPG1000, together with its parametric least-squares (LS) fit (red) using Eq. (4). For comparison, the best parametric fit for $\rho_1(h) = \sin(ah)/ah$ is also shown.

C. Interpretation of the parametric covariance model

The covariance function $\rho(h)$ in Eq. (4) used in this paper is the product of the covariance functions $\rho_1, \rho_2 : [0, \infty) \to \mathbb{R}$ defined by $\rho_1(h) = \sin(ah)/ah$ and $\rho_2(h) = \exp(-bh^2)$ for each $h > 0$ and model parameters $a, b > 0$.

For Gaussian excursion sets, covariance functions of the form ρ_1 lead to dendritic patterns in the modeled structures, see sec. 15.1 and Fig. 16.1 in Ref. [29]. However, based on the physicochemical theory of phase separation [53], random fields with such covariance functions have been used to model the morphology of spinodally decomposed materials, see, e.g., Refs. [39,54].

The nano-PGs considered in this paper, manufactured as stated in Sec. II A, can be described as spinodally decomposed materials. Nevertheless, one can clearly observe that the nonparametric estimator $\widehat{\rho}$ of ρ computed from tomographic image data, see Fig. 3, exhibits a faster decay than the best fit with ρ_1. A qualitatively similar effect has also been observed in spinodally decomposed Vycor glass, see Fig. 12 in Ref. [40]. Multiplying ρ_1 with the Gaussian-type covariance function ρ_2 allows for appropriately describing the covariance functions obtained from image data in our case. This leads to an exponential decay of $\rho = \rho_1 \rho_2$, where the influence of ρ_2 is stronger for larger values of the model parameter $b > 0$ introduced in Eq. (4).

For the expected surface area per unit volume S_Ξ of the excursion set Ξ with level $\lambda > 0$, analytical formulas are known. It is given by $S_\Xi = -4 \lim_{h \downarrow 0} C'(h)$, see eq. (6.164) in Ref. [41]. Under the assumption that ρ is twice differentiable, this leads to

$$S_\Xi = \frac{2}{\pi} \exp\left(\frac{-\lambda^2}{2}\right)\sqrt{-\rho''(0)},$$
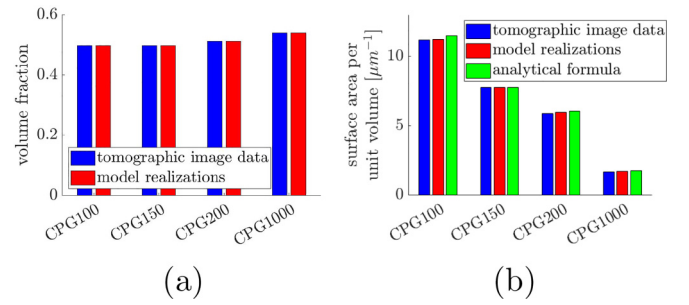

FIG. 4. Comparison of (a) volume fraction and (b) specific surface area computed from tomographic (blue) and simulated (red) image data. For the specific surface area, we also show the values (green) which have been obtained by the analytical formula given in Eq. (5).

see eq. (6.165) in Ref. [41]. The covariance functions considered in this paper, see Eq. (4), fulfill the differentiability assumption and we obtain

$$S_\Xi = \frac{2}{\pi\sqrt{3}} \exp\left(-\frac{\lambda^2}{2}\right)\sqrt{a^2 + 6b}. \tag{5}$$

This means that, for a given threshold λ, the value of S_Ξ is monotonously increasing in the parameters a and b, while for given a and b, it takes its maximum at $\lambda = 0$, i.e., at a porosity of $\varepsilon = 0.5$.

D. Model validation by morphological descriptors

The level-set model Ξ, which has been introduced in Sec. III A and calibrated by 3D image data in Sec. III B, is evaluated by considering various morphological descriptors of tomographic and simulated image data. More precisely, for each of the four samples CPG100, CPG150, CPG200, and CPG1000, we compare morphological descriptors computed from tomographic image data with the corresponding descriptors computed from model realizations, where we average over 10 realizations drawn from the calibrated model with a size of $400 \times 400 \times 400$ voxel. Note that, doing so, we generate virtual nanostructures of different physical sizes for each sample, see Table I for voxel and window sizes used for the different samples. This is reasonable since larger window sizes are needed for representation in the case of larger mean pore widths. The latter effect is illustrated in Fig. 1 and quantitatively represented by the covariance functions shown in Fig. 3.

First, we consider two classical morphological descriptors of binary image data: the volume fraction and the specific surface area, i.e., the expected surface area per unit volume, of the foreground phase. Recall that we use the point-count method to estimate volume fractions from voxelized data, see Sec. III B. Here, the local contribution to the surface area is determined based on weighted $2 \times 2 \times 2$ voxel configurations, which reduces the influence of the voxel size. To do this for the specific surface area, we exploit the algorithm described in Refs. [52,55]. For the fitted level-set models, we additionally compute the specific surface area by means of the analytical formula given in Eq. (5). The obtained results are visualized in Fig. 4. The good accordance between the values estimated
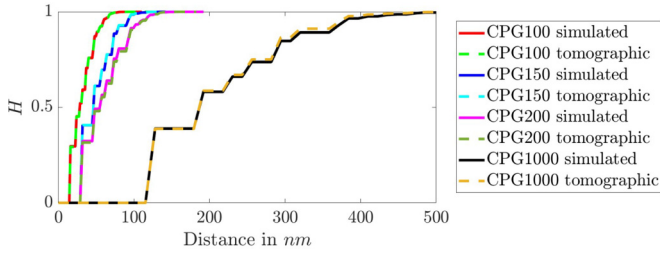
FIG. 5. Comparison of spherical contact distribution functions computed from tomographic and simulated image data.

from image data and the analytical ones can also be explained by the fact that the algorithm to estimate the surface area does not merely count the faces of voxels at the interface.

The volume fractions shown in Fig. 4 exhibit a nearly perfect fit. This is not surprising, as they are used to estimate the model parameter λ, see Sec. III B. The specific surface areas computed from simulated image data also nicely coincide with those computed from tomographic image data. Furthermore, similar values have been obtained by means of the analytical formula given in Eq. (5).

Additionally, we evaluate the level-set models by means of further morphological descriptors which have not been used for model fitting. To begin with, we consider the spherical contact distribution function $H : [0, \infty) \to [0, 1]$ of the pore space (see, e.g., Refs. [41,56,57]), where for each $r \geqslant 0$, the value of $H(r)$ is the (conditional) probability that the minimum distance from a randomly selected point of the pore phase Ξ^c to the solid phase Ξ is less or equal than r. Formally,

$$H(r) = 1 - \frac{\mathbb{E}[\nu_3(\Xi^c \ominus B(o, r))]}{1 - \varepsilon}, \qquad (6)$$

for each $r > 0$, where $B(o, r)$ denotes the ball with radius $r > 0$ centered in the origin and $\Xi^c \ominus B(o, r)$ denotes the morphological erosion of the pores space by the structuring element $B(o, r)$. Comparing the spherical contact distribution functions computed from tomographic image data with those of the simulated data shows an excellent fit for all four samples, see Fig. 5. For simulated data, the mean values over 10 realizations are shown. Note that the piecewise constant progression of the functions shown in Fig. 5 is due to the limited resolution of the underlying image data, cf. Table I.

Finally, we consider the mean geodesic tortuosity τ, which relies on the notion of geodesic distances introduced in Ref. [58], and the constrictivity β of the pore space, quantifying the strength of bottleneck effects [59]. Both quantities have a strong impact on effective transport properties such as effective diffusivity or permeability, see, e.g., Refs. [22,23]. The mean geodesic tortuosity is defined as the quotient of the expected length of the shortest paths through the material, which are fully contained in the phase under consideration, divided by the thickness of the material. However, note that there are various notions of tortuosity considered in the literature that differ from this definition, see Refs. [60–62] for an overview. Constrictivity is a morphological descriptor, which quantifies the strength of bottleneck effects within the nanostructure or microstructure under consideration. For geometrically complex morphologies, this descriptor was in-
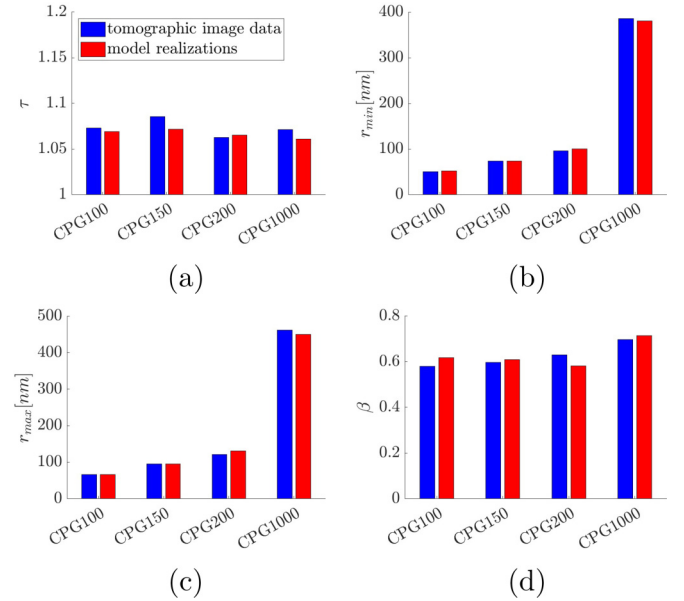

FIG. 6. Comparison of the transport relevant descriptors (a) τ, (b) $r_{\min}$, (c) $r_{\max}$, and (d) β computed from tomographic (blue) and simulated (red) image data.

troduced in Ref. [63], where it is defined by $\beta = r_{\min}^2/r_{\max}^2$. Here, $r_{\max} > 0$ is the maximum radius such that at least half of the pore space can be covered by (possibly overlapping) spheres with radius $r_{\max}$ that are fully contained in the pore space. In other words, $r_{\max}$ is defined as median of the continuous pore size distribution, which is computed via morphological opening of the pore space. Note that there is a one-to-one relationship, explicitly given in Ref. [36], between the continuous pore size distribution and the granulometry function from mathematical morphology [56].

On the other hand, $r_{\min} > 0$ is the maximum value such that half of the pore space can be reached by a ball with radius $r_{\min}$ intruding into the pore space from a predefined starting plane of the material. Thus, $\beta = r_{\min}^2/r_{\max}^2$ describes the strength of bottleneck effects within the pore space [22]. For a formal definition of the quantities τ, $r_{\min}$, $r_{\max}$, and β and their respective estimators in the framework of stationary random sets, we refer to Ref. [64]. Figure 6 shows the values of τ, $r_{\min}$, $r_{\max}$, and β computed from tomographic image data compared with the mean values of these descriptors computed from 10 realizations of the respective model. Again, the quantities computed from simulated image data nicely coincide with those computed from tomographic image data. Furthermore, in Table III, the mean values and standard deviations of τ, $r_{\min}$, $r_{\max}$, and β are given, along with the respective relative error compared to the corresponding values obtained from tomographic image data. Interestingly, for CPG100, CPG150, and CPG200, the value of $r_{\min}$ is nearly identical to half of the respective mean pore width, which is measured by mercury intrusion porosimetry and characterizes the different samples considered in this paper, cf. Sec. II A. This further justifies the use of $r_{\min}$ for purposes of model validation. A more detailed model validation is shown in Fig. 14, where the curves of simulated mercury intrusion porosimetries [59] are provided for measured image data and model realizations. These curves

TABLE III. Values of τ, $r_{\min}$, $r_{\max}$, and β estimated as an average of 10 model realizations, along with the respective standard deviations (std.) and the relative errors compared with the corresponding values obtained from tomographic image data.

	CPG100	CPG150	CPG200	CPG1000
τ	1.0693	1.0719	1.0653	1.0610
Std.	4.01×10^{-4}	1.76×10^{-4}	2.50×10^{-4}	2.04×10^{-4}
Error	0.36%	1.26%	0.24%	0.96%
$r_{\min}$[nm]	52.35	74.09	100.22	380.56
Std. [nm]	4.31×10^{-1}	3.22×10^{-2}	1.32	7.59×10^{-2}
Error	3.31%	1.03%	4.24%	1.27%
$r_{\max}$[nm]	66.60	94.95	131.38	450.12
Std. [nm]	6.91×10^{-3}	7.39×10^{-3}	1.44×10^{-2}	6.49×10^{-2}
Error	0.16%	0.10%	8.53%	2.54%
β	0.6179	0.6089	0.5820	0.7148
Std.	1.03×10^{-2}	4.98×10^{-4}	1.50×10^{-2}	1.07×10^{-4}
Error	6.39%	1.87%	7.74%	2.61%

TABLE IV. Mean values μ and standard deviations σ of model parameters estimated from 2D cross-sections of tomographic 3D image data and their respective relative errors compared with the values obtained for the corresponding 3D estimators based on the full tomographic datasets.

	CPG100	CPG150	CPG200	CPG1000
$\mu(\widehat{a}_{2D})$ [1/ μm]	27.01	18.9	15.31	3.874
$\sigma(\widehat{a}_{2D})$ [1/ μm]	0.72	1.4	0.22	0.24
Error	0.48%	1.70%	0.04%	0.66%
$\mu(\widehat{b}_{2D})$ [1/ μm^2]	37.12	15.16	5.796	1.250
$\sigma(\widehat{b}_{2D})$ [1/ μm^2]	3.9	4.1	0.69	0.20
Error	2.82%	1.97%	0.30%	1.49%
$\mu(\widehat{\lambda}_{2D})$	−0.0072	−0.0083	0.0320	0.1016
$\sigma(\widehat{\lambda}_{2D})$	0.041	0.048	0.038	0.032
Error	3.67%	9.91%	1.93%	1.20%
$\mu(\widehat{\varepsilon}_{2D})$	0.5029	0.5033	0.4873	0.4596
$\sigma(\widehat{\varepsilon}_{2D})$	0.016	0.019	0.015	0.013
Error	0.02%	0.06%	0.06%	0.09%

also show good accordance between simulated and measured data.

IV. MODEL CALIBRATION BY 2D IMAGE DATA

The ability to properly calibrate a stochastic 3D model by means of 2D image data is a great advantage for real-life applications, as the acquisition of tomographic 3D imaging is rather expensive in cost and time. Recall that the model parameters of random excursion sets induced by motion-invariant Gaussian random fields, considered in this paper, are uniquely defined by the volume fraction and the two-point coverage probabilities of the excursion sets. Moreover, these descriptors can even be reliably estimated based on one-dimensional (1D) information. Thus, it is possible to fit model parameters using 2D image data. Examples, where stochastic 3D models are fitted to 2D scanning electron microscopy (SEM) data of solid oxide fuel cells and composite silica materials can be found in Refs. [32,65], respectively.

We now explain how to calibrate the 3D level-set model Ξ, which has been introduced in Sec. III A, by means of individual 2D cross-sections of 3D image data and provide a discussion of the robustness of this procedure in the case of nano-PGs. Furthermore, the estimates obtained in this way for the model parameters are compared with the estimates obtained from 3D image data. For this, we fix an arbitrary 2D cross-section of the 3D image data (orthogonal to one of the three main axis directions). Note that the techniques described in Sec. III B for estimating the model parameters λ, a, and b from 3D image data can be directly applied to 2D data since the volume fraction and, due to the motion invariance of the level-set model Ξ, also the two-point coverage probabilities of Ξ can be estimated from 2D data. The estimators for ε, λ, a, and b obtained in this way will be denoted by $\widehat{\varepsilon}_{2D}$, $\widehat{\lambda}_{2D}$, $\widehat{a}_{2D}$, and $\widehat{b}_{2D}$, respectively. Furthermore, the averages of these 2D estimators for ε, λ, a, and b over all 2D cross-sections along the three main axis directions are denoted by $\mu(\widehat{\varepsilon}_{2D})$, $\mu(\widehat{\lambda}_{2D})$, $\mu(\widehat{a}_{2D})$, and $\mu(\widehat{b}_{2D})$.

Figure 7 shows the estimated probability densities of $\widehat{\varepsilon}_{2D}$, $\widehat{\lambda}_{2D}$, $\widehat{a}_{2D}$, and $\widehat{b}_{2D}$, which we obtained by kernel density es-

timation using the method described in Ref. [66]. Note that the estimator for ε is in a direct functional relationship to the estimator of λ through the cumulative distribution function of the normal distribution. However, this relationship is nonlinear, so that it is *a priori* unclear how it affects the variance and expectation of the corresponding estimators. We have therefore included the results on ε to assess the influence of the nonlinearity and to allow for an easier interpretation of the results through the more intuitive quantity ε. The mean values of these 2D estimates, together with their standard deviations and the respective relative errors compared with the values obtained for the corresponding 3D estimators, are provided in Table IV. Here, one can observe that, on average, the 2D estimators lead to nearly identical values as their 3D counterparts. However, the probability densities of the 2D estimates shown in Fig. 7 reveal that, for individual 2D cross-sections, the numerical differences between 2D estimators and 3D estimators can be relatively large. This is not surprising, as an individual 2D cross-section contains significantly less information than the complete 3D image. In this section, we only show the results which we obtained for the samples CPG150 and CPG200 since these are the samples with the highest and lowest sum of relative errors, respectively. The corresponding results obtained for CPG100 and CPG1000 are shown in Fig. 13.

Note that, from the results shown in Fig. 7 and Table IV, it cannot directly be concluded how the discrepancies in terms of the estimated model parameters λ, a, and b influence transport-relevant morphological descriptors, such as the tortuosity τ and the constrictivity β, of simulated image data drawn from level-set models for given values of $\widehat{\lambda}_{2D}$, $\widehat{a}_{2D}$, and $\widehat{b}_{2D}$. We quantitatively study this effect under the assumption that the volume fraction ε and, thus, the model parameter λ are estimated correctly. This is a reasonable assumption since, in many applications, the porosity ε can be reliably determined not only from image data but also by means of other experimental methods. The influence of the estimators $\widehat{a}_{2D}$ and $\widehat{b}_{2D}$ is investigated by means of a simulation study as follows.

For each sample, we generate virtual nanostructures for each of the following five specifications of the parameter vector (a, b): $(\mu(\widehat{a}_{2D}), \mu(\widehat{b}_{2D}))$, $(\mu(\widehat{a}_{2D}) + \sigma(\widehat{a}_{2D}), \mu(\widehat{b}_{2D}) + \sigma(\widehat{b}_{2D}))$, $(\mu(\widehat{a}_{2D}) + \sigma(\widehat{a}_{2D}), \mu(\widehat{b}_{2D}) - \sigma(\widehat{b}_{2D}))$, $(\mu(\widehat{a}_{2D}) - \sigma(\widehat{a}_{2D}), \mu(\widehat{b}_{2D}) + \sigma(\widehat{b}_{2D}))$, $(\mu(\widehat{a}_{2D}) - \sigma(\widehat{a}_{2D}), \mu(\widehat{b}_{2D}) - \sigma(\widehat{b}_{2D}))$, where $\sigma(\widehat{a}_{2D})$ and $\sigma(\widehat{b}_{2D})$ denote the standard deviation of $\widehat{a}_{2D}$ and $\widehat{b}_{2D}$, respectively, given in Table IV. Then we compute the tortuosity τ and the constrictivity β for simulated 3D image data drawn from the level-set models with these five specifications of (a, b) and compare the obtained values with the values of τ and β computed for realizations of the level-set model Ξ calibrated by means of tomographic (3D) image data and for the tomographic image data itself. The results obtained in this way for the samples CPG150 and CPG200 are shown in Fig. 8. The corresponding results for CPG100 and CPG1000 are shown in Fig. 12.

Except for the constrictivity β of sample CPG150, the values obtained for τ and β, when calibrating the level-set model Ξ by tomographic (3D) image data, are accurately reproduced by the modified models, for which the parameter vector (a, b) is chosen as described above, i.e., by adding or subtracting the corresponding standard deviations to/from the averages of the estimators $\widehat{a}_{2D}$ and $\widehat{b}_{2D}$. The good accordance for CPG200, see Fig. 8(d), can be attributed to the fact that the values of $\widehat{a}_{2D}$ and $\widehat{b}_{2D}$ computed from individual 2D slices have only small deviations from the corresponding 3D estimates, see Table IV. In general, one can observe that the constrictivity β is much more sensitive to changes in the model parameters a and b than mean geodesic tortuosity τ. This is most visible for sample CPG150, see Fig. 8. Here, the difference between the parameters a and b estimated from 2D data and those estimated from 3D data cause considerable deviations in constrictivity β, while the tortuosity τ is almost entirely unaffected.

V. RELATIONSHIPS BETWEEN MEAN PORE WIDTH AND THE ENTIRE 3D MORPHOLOGY

In this section, we use the calibrated stochastic 3D model to quantify relationships between the mean pore width, which can be adjusted during the manufacturing process, and the entire 3D morphology. In doing so, we aim at simulating the morphology of nano-PGs, for which no 3D image data are available or which have not even been manufactured so far. For this purpose, we proceed similarly as in Refs. [67,68], i.e., we quantify relationships between mean pore width and model parameters to predict the 3D morphology of PG with a predefined mean pore width.

Recall that the CPG samples considered in this paper are labeled according to their respective mean pore widths of 100, 150, 200, and 1000 nm, which have been determined by means of mercury intrusion porosimetry. For quantifying relationships between the mean pore width and the parameter vector (a, b) of the covariance function of the underlying Gaussian random field X, see Sec. III B, it turns out that parametric functions of the form $f : [0, \infty) \rightarrow [0, \infty)$, given by
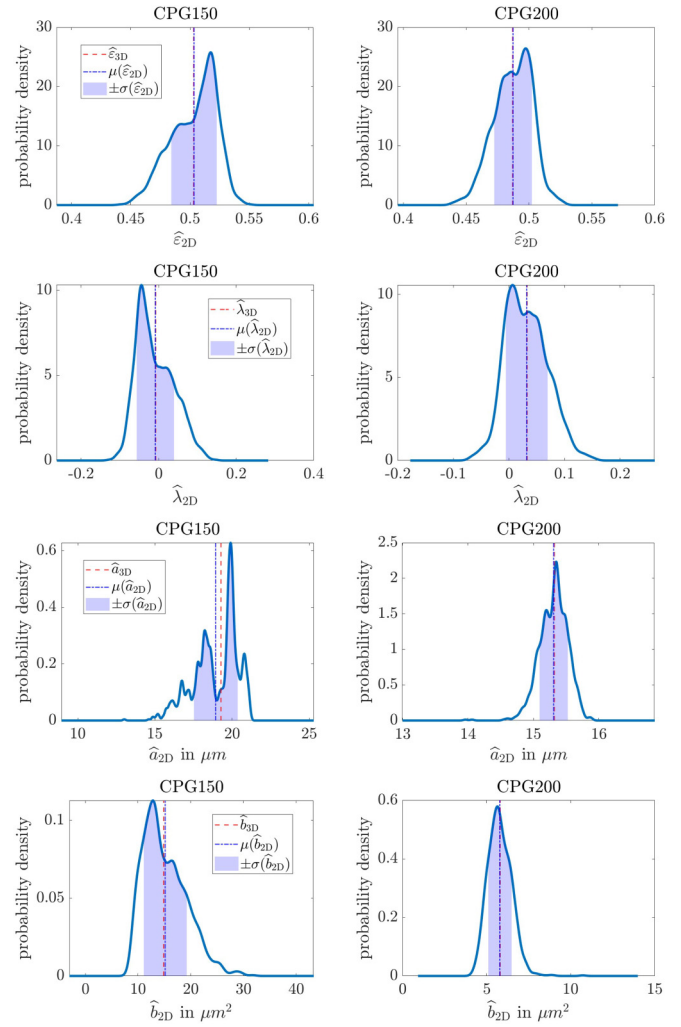
$$f(x) = c^{(1)} \exp(-c^{(2)}x) + c^{(3)}, \tag{7}$$

FIG. 7. Probability densities of the values obtained for $\widehat{\varepsilon}_{2D}$, $\widehat{\lambda}_{2D}$, $\widehat{a}_{2D}$, and $\widehat{b}_{2D}$, respectively, for all two-dimensional (2D) cross-sections along the three main axis directions. The vertical lines show the respective averages $\mu(\widehat{\varepsilon}_{2D})$, $\mu(\widehat{\lambda}_{2D})$, $\mu(\widehat{a}_{2D})$, and $\mu(\widehat{b}_{2D})$ (blue), and the values obtained for the corresponding three-dimensional (3D) estimators (red).

for each $x \geqslant 0$, are an appropriate tool. Here, x represents the mean pore width of the material under consideration, and $f(x)$ is the best predicted value of the model parameters a and b, respectively, given that the mean pore width is equal to x. We determine $c_a^{(1)}, c_a^{(2)}, c_a^{(3)} > 0$ and $c_b^{(1)}, c_b^{(2)}, c_b^{(3)} > 0$ for predicting the parameters a and b, respectively, by least-squares fitting based on the values given in Table II, which yields $c_a^{(1)} = 0.04703$, $c_a^{(2)} = 0.007238$, $c_a^{(3)} = 0.0039$, $c_b^{(1)} = 2.791 \times 10^{-4}$, $c_b^{(2)} = 0.02019$, and $c_b^{(3)} = 1.158 \times 10^{-6}$. The corresponding prediction functions are denoted by f_a and f_b. Moreover, note that inserting the parameters $a = f_a(x)$ and $b = f_b(x)$ predicted by the functions given in Eq. (7) with these regression coefficients into Eq. (5) yields a prediction for the specific surface area S_Ξ, where we assume a porosity of $\varepsilon = 0.5$ for all mean pore widths, see Fig. 9.

Model realizations with intermediate mean pore widths based on the predicted parameters a and b are visualized in Fig. 10, with an assumed porosity of $\varepsilon = 0.5$.
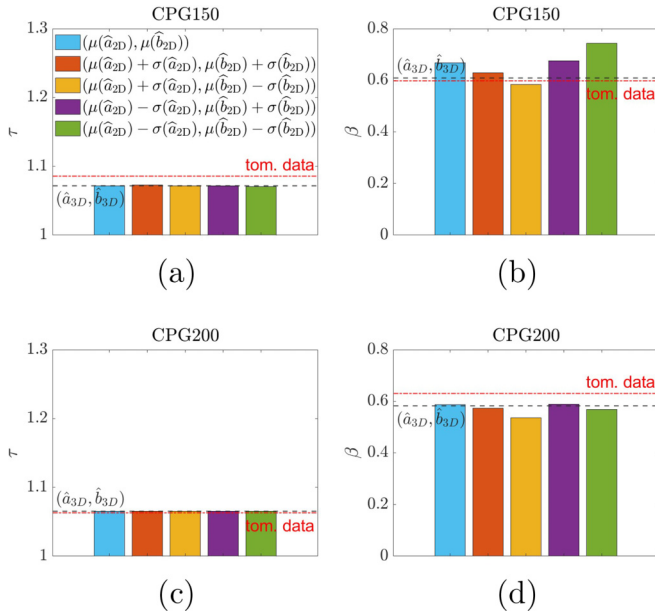
FIG. 8. (a) Tortuosity and (b) constrictivity for CPG150 and as well as (c) tortuosity and (d) constrictivity for CPG200, computed from simulated three-dimensional (3D) image data drawn from level-set models with different specifications of (a, b), together with the corresponding values estimated from tomographic image data.

Using the idea of cross-validation, see sec. 7.10 in Ref. [69], we assess the predictive power of the regression model given in Eq. (7), where the coefficients $c_a^{(1)}, c_a^{(2)}, c_a^{(3)}, c_b^{(1)}, c_b^{(2)}$, and $c_b^{(3)}$ are now fitted twice, in each case based on three samples only, i.e., disregarding CPG150 and CPG200, respectively. Then we evaluate the accuracy of the relationships given in Eq. (7), where the regression coefficients $c_a^{(1)}, c_a^{(2)}, c_a^{(3)}, c_b^{(1)}, c_b^{(2)}$, and $c_b^{(3)}$ are computed as described above. We compare the values obtained in this way for the model parameters a and b for the mean pore widths of 150 and 200 nm with the estimates $\widehat{a}$ and $\widehat{b}$ computed from tomographic (3D) image data for CPG150 and CPG200, as described in Sec. III B. Here, we obtain relative errors of 4.27 and 4.35% for a and b of CPG150 and 7.38 and 8.00% for a and b of CPG200, respectively. This shows that the interpolated model parameters are close to those estimated from tomographic image data. The regression curves fitted without

one of the samples CPG150 and CPG200 are provided in the Appendix, see Fig. 15.

Based on the model parameters a and b obtained from these regression models, we generate new (simulated) 3D morphologies for CPG150 and CPG20. Furthermore, we compare the average values of the transport-relevant descriptors τ, $r_{\min}$, $r_{\max}$, and β obtained for 10 realizations of these 3D morphologies with those obtained for 10 realizations of simulated 3D morphologies, where a and b have been estimated from tomographic (3D) image data for CPG150 and CPG20 as described in Sec. III B, as well as with those values of τ, $r_{\min}$, $r_{\max}$, and β directly computed from tomographic image data, see Fig. 11. The results obtained in this way show that the simulated 3D morphologies for regression- and image-based estimates of the model parameters a and b are overall similar to those of tomographic image data. This validates our prediction formulas. However, when applying the proposed prediction formulas, one should keep in mind that regression is performed with only four data points here.

VI. CONCLUSIONS

In this paper, we developed and calibrated a stochastic 3D model for differently manufactured nano-PGs based on tomographic x-ray image data. Model validation is performed by comparing morphological descriptors computed from model realizations and image data, which are not used for model calibration and are nevertheless matched with a high degree of accuracy. We want to emphasize that the utilized model, which is based on methods of stochastic geometry, has certain advantages in comparison with nonparametric or high-dimensional generative models, see also the discussion in Ref. [70]. Namely, it is fully determined by three parameters only, which allows us to physically interpret their values. Moreover, we discuss the form of the correlation functions of the underlying Gaussian random field and relate them to the manufacturing process.

We also show that the model can be reliably calibrated merely based on 2D information in the form of image cross-sections taken from the complete 3D image data. Our analysis showed that the average calibration over multiple cross-sections leads to nearly identical results compared with the calibration based on 3D image data. This means that, for model calibration, a collection of sufficiently many 2D images can replace the need for the acquisition of tomographic
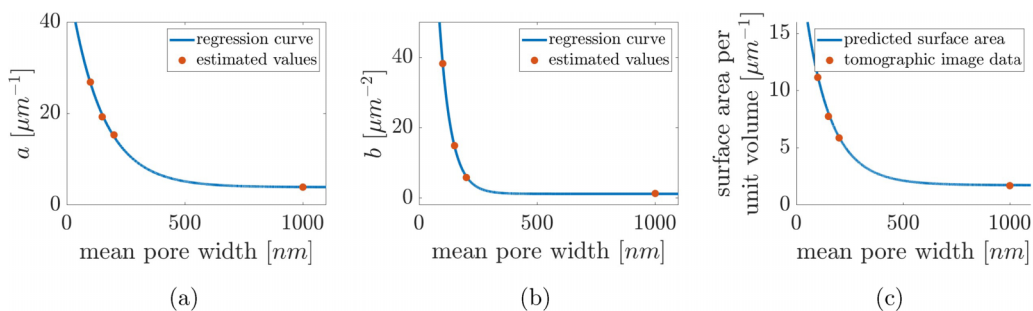

FIG. 9. Regression curves for predicting the model parameters (a) a and (b) b for mean pore widths, for which no three-dimensional (3D) image data are available. (c) Prediction of specific surface area using a combination of Eq. (5) with the relationships between mean pore width and model parameters.

3D image data. However, the variance among different 2D cross-sections is not negligible and can have a large impact on sensitive morphological descriptors, such as constrictivity, which introduces a significant uncertainty if model calibration is based only on single cross-sections.

The available image data covered samples of nano-PG with different mean pore widths. By means of a parametric regression, we were able to quantify the relationship between the mean pore width, which can be adjusted in the manufacturing process, and the resulting morphological descriptors. This, in turn, allows us to interpolate between the available data samples and to predict virtual 3D morphologies with intermediate mean pore widths that have not been manufactured so far. We validated our predictive simulations by means of cross-validation, which showed that using a subset of the available samples to predict the properties of the remaining samples leads to accurate results. A reliable virtual prediction of nano-PG with predefined pore widths opens possibilities for a resource efficient optimization of the 3D morphology of nano-PG. More precisely, it allows for optimizing the mean pore widths with respect to morphological descriptors that cannot directly be adjusted during the manufacturing process. Furthermore, combining stochastic modeling with numerical simulation can be used in future work to optimize the mean pore width with respect to physical properties like effective diffusivity.

ACKNOWLEDGMENTS

APPENDIX

We provide plots analogous to those of Figs. 7 and 8 for the remaining samples CPG100 and CPG1000 which are not shown in the main text, see Figs. 12 and 13. Figure 14
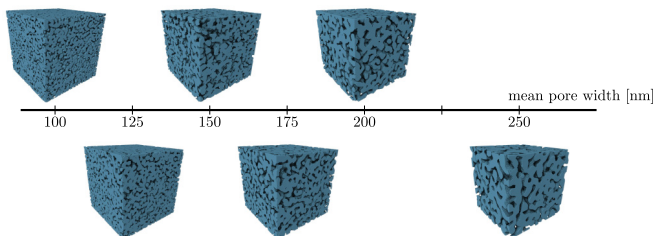

FIG. 10. Top row: Three-dimensional (3D) renderings of tomographic image data for mean pore widths of 100, 150, and 200 nm. Bottom row: Predictively simulated 3D morphologies for mean pore widths of 125, 175, and 250 nm.
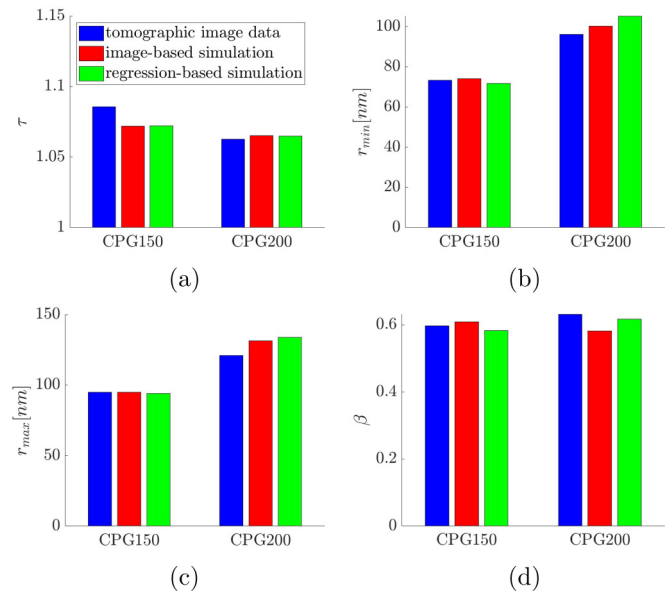

FIG. 11. Comparison of the transport-relevant descriptors (a) τ, (b) $r_{\min}$, (c) $r_{\max}$, and (d) β, computed from simulated three-dimensional (3D) morphologies for regression-based (red) and image-based (green) estimates of the model parameters a and b, as well as directly computed from tomographic image data (blue).

shows curves of simulated mercury intrusion porosimetry for both tomographic image data and model realizations. The simulation was performed along each main axis direction and then averaged for visualization. The 50th percentile of this curve is used in the definition of $r_{\min}$, which in turn appears in the definition of the constrictivity β. The plots of the
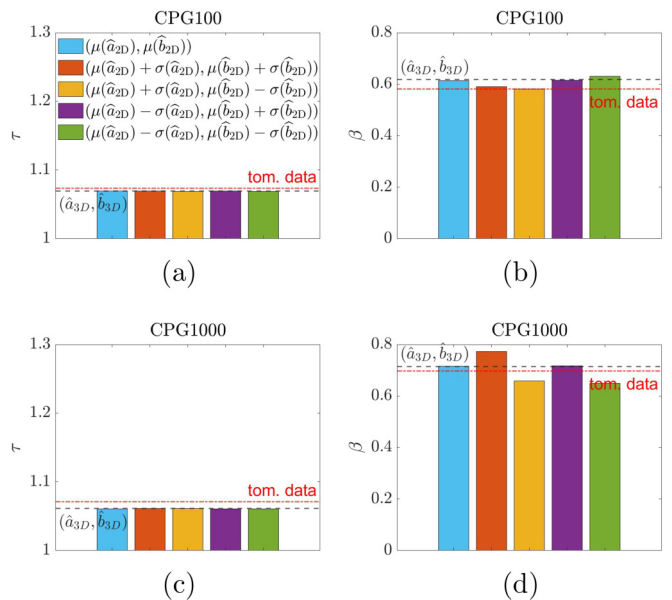

FIG. 12. (a) Tortuosity and (b) constrictivity for CPG100 and as well as (c) tortuosity and (d) constrictivity for CPG1000, computed from simulated three-dimensional (3D) image data drawn from level-set models with different specifications of (a, b), together with the corresponding values estimated from tomographic image data.
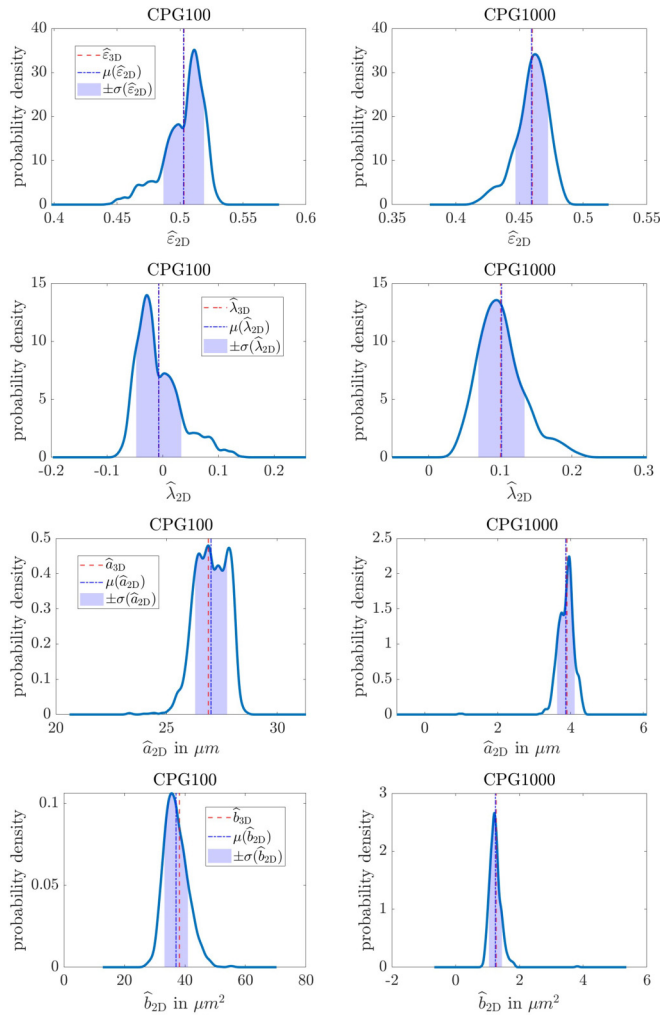
FIG. 13. Probability densities of the values obtained for $\widehat{\varepsilon}_{2D}$, $\widehat{\lambda}_{2D}$, $\widehat{a}_{2D}$, and $\widehat{b}_{2D}$, respectively, for all two-dimensional (2D) cross-sections along the three main axis directions. The vertical lines show the respective averages $\mu(\widehat{\varepsilon}_{2D})$, $\mu(\widehat{\lambda}_{2D})$, $\mu(\widehat{a}_{2D})$, and $\mu(\widehat{b}_{2D})$ (blue) and the values obtained for the corresponding three-dimensional (3D) estimators (red).

regression curves are shown in Fig. 15, which are used for cross-validation of the predictive simulations considered in Sec. V. In Fig. 16, we also provide the chord-length distribution functions, see sec. 6.3.4 in Ref. [41], computed for the
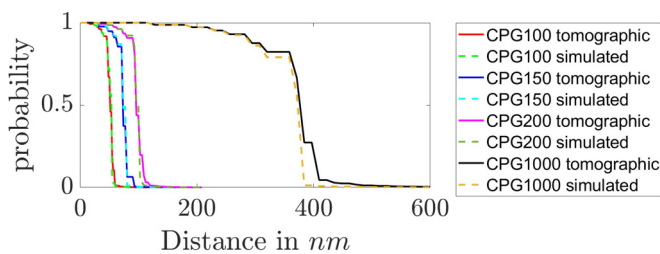

FIG. 14. Simulated mercury intrusion porosimetry computed from tomographic and simulated image data. The simulation was performed along the direction of each major axis and averaged for visualization.
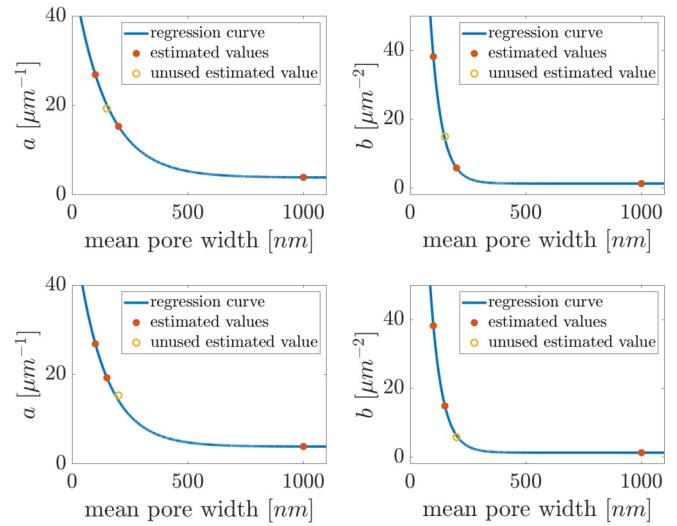

FIG. 15. Regression curves for predicting the model parameters a (left) and b (right) for mean pore widths, for which no three-dimensional (3D) image data are available, disregarding CPG150 (top row) and CPG200 (bottom row), respectively.

tomographic image data along the three main axis directions. For a predefined direction, the chord-length distribution function is the distribution function of the typical segment in this direction, which is completely contained in the glass phase. In the case of isotropy, the chord-length distribution functions in all directions coincide. Figure 16 shows that, for all samples considered in this paper, the chord-length distribution functions in the three main axis directions are nearly identical. This confirms the assumption of structural isotropy motivated by the manufacturing process.
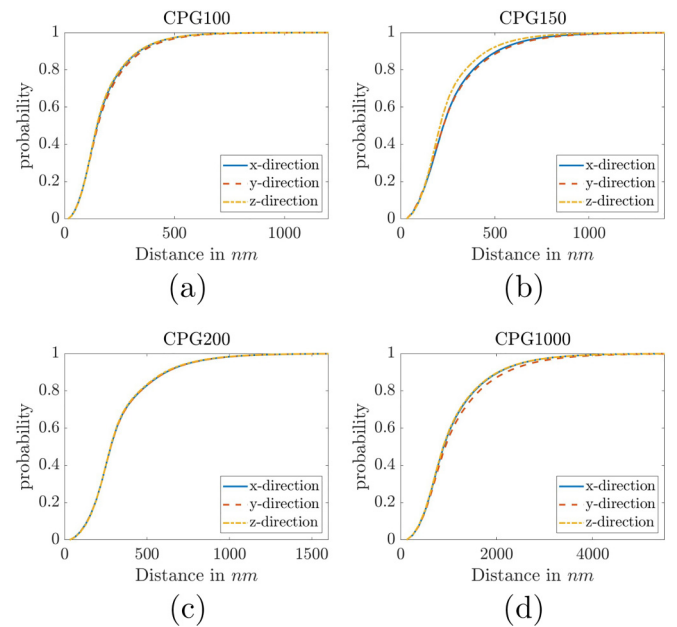

FIG. 16. Chord-length distribution functions of the samples (a) CPG100, (b) CPG150, (c) CPG200, and (d) CPG1000 along the three major axes. With respect to this geometrical descriptor, the data show no signs of anisotropy.

[1] D. Enke, F. Janowski, and W. Schwieger, Porous glasses in the 21st century—a short review, Microporous Mesoporous Mater. **60**, 19 (2003).

[2] A. Shakhov, C. Reichenbach, D. Kondrashova, P. Zeigermann, D. Mehlhorn, D. Enke, and R. Valiullin, Exploring internal structure of nanoporous glasses obtained by leaching of phase-separated alkali borosilicate glasses, Chem. Ing. Tech. **85**, 1734 (2013).

[3] S. Gruener, T. Hofmann, D. Wallacher, A. V. Kityk, and P. Huber, Capillary rise of water in hydrophilic nanopores, Phys. Rev. E **79**, 067301 (2009).

[4] P. Huber, Soft matter in hard confinement: phase transition thermodynamics, structure, texture, diffusion and flow in nanoporous media, J. Phys.: Condens. Matter **27**, 103102 (2015).

[5] B. Maillet, G. Dittrich, P. Huber, and P. Coussot, Diffusionlike drying of a nanoporous solid as revealed by magnetic resonance imaging, Phys. Rev. Appl. **18**, 054027 (2022).

[6] D. Gruszka, S. Schmid, and C. Dekker, Nanopores: a versatile tool to study protein dynamics, Essays Biochem. **65**, 93 (2021).

[7] S. Hayashi, K. Ito, M. Nonoguchi, Y. Takasaki, and K. Imada, Immobilization of a fructosyl-transferring enzyme from *aureobasidium* sp. on *shirasu* porous glass, J. Ferment. Bioeng. **72**, 68 (1991).

[8] A. A. Tsygankov, Y. Hirata, M. Miyake, Y. Asada, and J. Miyake, Photobioreactor with photosynthetic bacteria immobilized on porous glass for hydrogen photoproduction, J. Ferment. Bioeng. **77**, 575 (1994).

[9] F. Baumann, T. Paul, S. Wassersleben, R. Regenthal, D. Enke, and A. Aigner, Characterization of drug release from mesoporous SiO_2-based membranes with variable pore structure and geometry, Pharmaceutics **14**, 1184 (2022).

[10] C. J. Brinker and G. W. Scherer, *Sol-Gel Science: The Physics and Chemistry of Sol-Gel Processing* (Academic Press, San Diego, 2013).

[11] T. H. Elmer, Porous and reconstructed glasses, in *Engineered Materials Handbook, Vol. 4: Ceramics and Glasses*, ASM International, edited by S. J. Schneider (CRC Press, Materials Park, 1991), pp. 427–432.

[12] D. Enke, R. Gläser, and U. Tallarek, Sol-gel and porous glass-based silica monoliths with hierarchical pore structure for solid-liquid catalysis, Chem. Ing. Tech. **88**, 1561 (2016).

[13] A. Inayat, B. Reinhardt, J. Herwig, C. Küster, H. Uhlig, S. Krenkel, E. Rädlein, and D. Enke, Recent advances in the synthesis of hierarchically porous silica materials on the basis of porous glasses, New J. Chem. **40**, 4095 (2016).

[14] H. Enninful, D. Schneider, D. Enke, and R. Valiullin, Impact of geometrical disorder on phase equilibria of fluids and solids confined in mesoporous materials, Langmuir **37**, 3521 (2021).

[15] D. Mehlhorn, D. Kondrashova, C. Küster, D. Enke, T. Emmerich, A. Bunde, R. Valiullin, and J. Kärger, Diffusion in complementary pore spaces, Adsorption **22**, 879 (2016).

[16] N. Sonnenberger, N. Anders, Y. Golitsyn, M. Steinhart, D. Enke, K. Saalwächter, and M. Beiner, Pharmaceutical nanocrystals confined in porous host systems—interfacial effects and amorphous interphases, Chem. Commun. **52**, 4466 (2016).

[17] P. Huber and K. Knorr, Adsorption-desorption isotherms and x-ray diffraction of ar condensed into a porous glass matrix, Phys. Rev. B **60**, 12657 (1999).

[18] D. Wallacher, R. Ackermann, P. Huber, M. Enderle, and K. Knorr, Diffraction study of solid oxygen embedded in porous glasses, Phys. Rev. B **64**, 184203 (2001).

[19] M. Neumann, O. Furat, D. Hlushkou, U. Tallarek, L. Holzer, and V. Schmidt, On microstructure-property relationships derived by virtual materials testing with an emphasis on effective conductivity, in *Simulation Science: First International Workshop, SimScience 2017, Göttingen, Germany, April 27-28, 2017, Revised Selected Papers*, edited by M. Baum, G. Brenner, J. Grabowski, T. Hanschke, S. Hartmann, and A. Schöbel (Springer, Berlin, 2018), pp. 145–158.

[20] S. Barman, H. Rootzén, and D. Bolin, Prediction of diffusive transport through polymer films from characteristics of the pore geometry, AIChE J. **65**, 446 (2019).

[21] O. Birkholz, M. Neumann, V. Schmidt, and M. Kamlah, Stochastic microstructure modeling and numerical simulation of effective electronic conductivity of aggregated particles in hierarchically structured electrodes, Powder Technol. **378**, 659 (2021).

[22] M. Neumann, O. Stenzel, F. Willot, L. Holzer, and V. Schmidt, Quantifying the influence of microstructure on effective conductivity and permeability: Virtual materials testing, Int. J. Solids Struct. **184**, 211 (2020).

[23] B. Prifling, M. Röding, P. Townsend, M. Neumann, and V. Schmidt, Large-scale statistical learning for mass transport prediction in porous materials using 90,000 artificially generated microstructures, Front. Mater. **8**, 786502 (2021).

[24] M. Röding, Z. Ma, and S. Torquato, Predicting permeability via statistical learning on higher-order microstructural information, Sci. Rep. **10**, 15239 (2020).

[25] S. Gruener, Z. Sadjadi, H. E. Hermes, A. V. Kityk, K. Knorr, S. U. Egelhaaf, H. Rieger, and P. Huber, Anomalous front broadening during spontaneous imbibition in a matrix with elongated pores, Proc. Natl. Acad. Sci. USA **109**, 10245 (2012).

[26] S. Gruener, H. E. Hermes, B. Schillinger, S. U. Egelhaaf, and P. Huber, Capillary rise dynamics of liquid hydrocarbons in mesoporous silica as explored by gravimetry, optical and neutron imaging: Nano-rheology and determination of pore size distributions from the shape of imbibition fronts, Colloids Surf., A **496**, 13 (2016).

[27] D. Enke, F. Friedel, F. Janowski, T. Hahn, W. Gille, R. Müller, and H. Kaden, Ultrathin porous glass membranes with controlled texture properties, in *Characterization of Porous Solids VI: Proceedings of the 6th International Symposium on the Characterization of Porous Solids (COPS-VI)*, edited by F. Rodriguez-Reinoso, J. McEnaney, B. Rouquerol, and K. Unger, Studies in Surface Science and Catalysis Vol. 144 (Elsevier, Amsterdam, 2002), pp. 347–354.

[28] R. Kohns, C. P. Haas, A. Höltzel, C. Splith, D. Enke, and U. Tallarek, Hierarchical silica monoliths with submicron macropores as continuous-flow microreactors for reaction kinetic and mechanistic studies in heterogeneous catalysis, React. Chem. Eng. **3**, 353 (2018).

[29] C. Lantuéjoul, *Geostatistical Simulation: Models and Algorithms* (Springer, Berlin, 2002).

[30] L. D. Gelb and K. E. Gubbins, Characterization of porous glasses: Simulation models, adsorption isotherms, and the Brunauer-Emmett-Teller analysis method, Langmuir **14**, 2097 (1998).

[31] L. D. Gelb and K. E. Gubbins, Pore size distributions in porous glasses: A computer simulation study, Langmuir **15**, 305 (1999).

[32] B. Abdallah, F. Willot, and D. Jeulin, Morphological modelling of three-phase microstructures of anode layers using SEM images, J. Microsc. **263**, 51 (2016).

[33] H. Moussaoui, J. Laurencin, Y. Gavet, G. Delette, M. Hubert, P. Cloetens, T. Le Bihan, and J. Debayle, Stochastic geometrical modeling of solid oxide cells electrodes validated on 3D reconstructions, Comput. Mater. Sci. **143**, 262 (2018).

[34] H. Moussaoui, R. K. Sharma, J. Debayle, Y. Gavet, G. Delette, and J. Laurencin, Microstructural correlations for specific surface area and triple phase boundary length for composite electrodes of solid oxide cells, J. Power Sources **412**, 736 (2019).

[35] M. Neumann, B. Abdallah, L. Holzer, F. Willot, and V. Schmidt, Stochastic 3D modeling of three-phase microstructures for the prediction of transport properties in solid oxide fuel cells, Transp. Porous Media **128**, 179 (2019).

[36] M. Neumann, M. Osenberg, A. Hilger, D. Franzen, T. Turek, I. Manke, and V. Schmidt, On a pluri-gaussian model for three-phase microstructures, with applications to 3D image data of gas-diffusion electrodes, Comput. Mater. Sci. **156**, 325 (2019).

[37] J. Quintanilla, R. F. Reidy, B. P. Gorman, and D. W. Mueller, Gaussian random field models of aerogels, J. Appl. Phys. **93**, 4584 (2003).

[38] E. Roubin, J.-B. Colliat, and N. Benkemoun, Meso-scale modeling of concrete: A morphological description based on excursion sets of random fields, Comput. Mater. Sci. **102**, 183 (2015).

[39] C. Soyarslan, S. Bargmann, M. Pradas, and J. Weissmüller, 3D stochastic bicontinuous microstructures: Generation, topology and elasticity, Acta Mater. **149**, 326 (2018).

[40] P. Levitz, Off-lattice reconstruction of porous media: Critical evaluation, geometrical confinement and molecular transport, Adv. Colloid Interface Sci. **76-77**, 71 (1998).

[41] S. N. Chiu, D. Stoyan, W. S. Kendall, and J. Mecke, *Stochastic Geometry and its Applications*, 3rd ed. (J. Wiley & Sons, Chichester, 2013).

[42] D. Jeulin, *Morphological Models of Random Structures* (Springer, Cham, 2021).

[43] S. Kench and S. J. Cooper, Generating three-dimensional structures from a two-dimensional slice with generative adversarial network-based dimensionality expansion, Nat. Mach. Intell. **3**, 299 (2021).

[44] C. L. Y. Yeong and S. Torquato, Reconstructing random media, Phys. Rev. E **57**, 495 (1998).

[45] M. V. Karsanina and K. M. Gerke, Hierarchical optimization: Fast and robust multiscale stochastic reconstructions with rescaled correlation functions, Phys. Rev. Lett. **121**, 265501 (2018).

[46] A. Cherkasov, A. Ananev, M. Karsanina, A. Khlyupin, and K. Gerke, Adaptive phase-retrieval stochastic reconstruction with correlation functions: Three-dimensional images from two-dimensional cuts, Phys. Rev. E **104**, 035304 (2021).

[47] D. P. Bentz, E. J. Garboczi, and D. A. Quenard, Modelling drying shrinkage in reconstructed porous materials: application to porous Vycor glass, Modell. Simul. Mater. Sci. Eng. **6**, 211 (1998).

[48] B. Jähne, *Digital Image Processing*, 6th ed. (Springer, Berlin, 2013).

[49] A. Buades, B. Coll, and J.-M. Morel, A non-local algorithm for image denoising, in *IEEE Computer Society Conference on Computer Vision and Pattern Recognition (CVPR 05), San Diego, CA, USA* (IEEE, San Diego, CA, 2005), Vol. 2, pp. 60–65.

[50] C. S. de Oliveira, R. Kohns, F. Meyerhöfer, S. Carstens, D. Enke, R. B. Wehrspohn, and J. Martins de Souza e Silva, Multi-technique structural characterization of glass foams with complex pore structures obtained through phase separation, Mater. Chem. Front. **5**, 4615 (2021).

[51] R. J. Adler, *The Geometry of Random Fields* (J. Wiley & Sons, Chichester, 1981).

[52] J. Ohser and K. Schladitz, *3D Images of Materials Structures: Processing and Analysis* (J. Wiley & Sons, Weinheim, 2009).

[53] J. W. Cahn, Phase separation by spinodal decomposition in isotropic systems, J. Chem. Phys. **42**, 93 (1965).

[54] S. Kumar, S. Tan, L. Zheng, and D. M. Kochmann, Inverse-designed spinodoid metamaterials, npj Comput. Mater. **6**, 73 (2020).

[55] K. Schladitz, J. Ohser, and W. Nagel, Measuring intrinsic volumes in digital 3D images, in *13th International Conference Discrete Geometry for Computer Imagery*, edited by A. Kuba, L. Nyúl, and K. Palágyi (Springer, Berlin, 2007), pp. 247–258.

[56] G. Matheron, *Random Sets and Integral Geometry* (J. Wiley & Sons, New York, 1975).

[57] J. Serra, *Image Analysis and Mathematical Morphology* (Academic Press, London, 1982).

[58] C. Lantuéjoul and F. Maisonneuve, Geodesic methods in quantitative image analysis, Pattern Recognition **17**, 177 (1984).

[59] L. Holzer, D. Wiedenmann, B. Münch, L. Keller, M. Prestat, P. Gasser, I. Robertson, and B. Grobéty, The influence of constrictivity on the effective transport properties of porous layers in electrolysis and fuel cells, J. Mater. Sci. **48**, 2934 (2013).

[60] M. B. Clennell, Tortuosity: a guide through the maze, Geol. Soc. Spec. Publ. **122**, 299 (1997).

[61] B. Ghanbarian, A. G. Hunt, R. P. Ewing, and M. Sahimi, Tortuosity in porous media: A critical review, Soil Sci. Soc. Am. J. **77**, 1461 (2013).

[62] L. Holzer, P. Marmet, M. Fingerle, A. Wiegmann, M. Neumann, and V. Schmidt, *Tortuosity and Microstructure Effects in Porous Media: Classical Theories, Empirical Data and Modern Methods* (Springer, Cham, 2023).

[63] L. Holzer, B. Iwanschitz, T. Hocker, L. Keller, O. M. Pecho, G. Sartoris, P. Gasser, and B. Münch, Redox cycling of Ni–YSZ anodes for solid oxide fuel cells: Influence of tortuosity, constriction and percolation factors on the effective transport properties, J. Power Sources **242**, 179 (2013).

[64] M. Neumann, C. Hirsch, J. Staněk, V. Beneš, and V. Schmidt, Estimation of geodesic tortuosity and constrictivity in stationary random closed sets, Scand. J. Stat. **46**, 848 (2019).

[65] Z. Jiang, W. Chen, and C. Burkhart, Efficient 3D porous microstructure reconstruction via gaussian random field and hybrid optimization, J. Microsc. **252**, 135 (2013).

[66] Z. I. Botev, J. F. Grotowski, and D. P. Kroese, Kernel density estimation via diffusion, Ann. Statist. **38**, 2916 (2010).

[67] B. Prifling, D. Westhoff, V. Schmidt, H. Markötter, I. Manke, V. Knoblauch, and V. Schmidt, Parametric microstructure mod-

eling of compressed cathode materials for Li-ion batteries, Comput. Mater. Sci. **169**, 109083 (2019).

[68] D. Westhoff, J. J. Van Franeker, T. Brereton, D. P. Kroese, R. A. J. Janssen, and V. Schmidt, Stochastic modeling and predictive simulations for the microstructure of organic semiconductor films processed with different spin coating velocities, Modell. Simul. Mater. Sci. Eng. **23**, 045003 (2015).

[69] T. Hastie, R. Tibshirani, and J. Friedman, *The Elements of Statistical Learning*, 2nd ed. (Springer, New York, 2008).

[70] X. Emery and C. Lantuéjoul, Can a training image be a substitute for a random field model? Math. Geosci. **46**, 133 (2014).